Check for updates

Advanced Functional Materials

ADVANCED FUNCTIONAL MATERIALS
www.afm-journal.de

RESEARCH ARTICLE

Biomimetic Gradient Microstructures Enable Stable, High-Sensitivity Pressure Sensing From Pa to MPa

Boru Jin[1,2] | Rongjie Zhuang[3] | Zhonglong Zhang[2] | Boning Sun[4] | Wenchao Gao[2] | Caofeng Pan[1,4]

[1]Center on Nanoenergy Research, Institute of Science and Technology for Carbon Peak and Neutrality, Key Laboratory of Blue Energy and Systems Integration (Guangxi University), Education Department of Guangxi Zhuang Autonomous Region, School of Physical Science and Technology, Guangxi University, Nanning, People's Republic of China | [2]Beijing Institute of Nanoenergy and Nanosystems, Chinese Academy of Sciences, Beijing, People's Republic of China | [3]College of Materials and Metallurgy, Guizhou University, Guiyang, People's Republic of China | [4]Beijing Key Laboratory for Atomic Manufacturing Equipment and Intelligent Sensing, Institute of Atomic Manufacturing, Beihang University, Beijing, People's Republic of China

Correspondence: Wenchao Gao (gaowenchao@binn.cas.cn) | Caofeng Pan (pancaofeng@buaa.edu.cn)

Received: 25 April 2026 | **Revised:** 2 July 2026 | **Accepted:** 22 July 2026

Keywords: finite element analysis | gradient hemispherical array | high sensitivity | interpretable machine learning | stable linear response

ABSTRACT

Flexible pressure sensors are often evaluated over only a limited portion of their nominal operating range, making it difficult to simultaneously achieve high-sensitivity, ultrawide- range detection, and reliable signal resolution under large preloads within a single device. Here, we present a geometry-guided strategy for stable pressure sensing from Pa to MPa based on a biomimetic daisy-inspired gradient hemispherical array. By integrating finite-element-analysis-guided optimization with an interpretable simulation-trained surrogate model, the multilevel gradient microstructure is rationally engineered to regulate compressibility and contact-area evolution, thereby mitigating capacitive saturation and extending the accessible pressure range. The resulting iontronic sensor delivers a consistently high sensitivity exceeding 122 kPa^{-1} over 0–2555 kPa, together with an ultrahigh sensitivity of 1864 kPa^{-1} in the low-pressure regime (0–61 kPa) and a low detection limit of 7.6 Pa. The device further shows fast response/recovery times below 5 ms, stable operation under repeated loading, and reliable pressure resolution even under MPa-level preloads. Beyond device performance, the surrogate-model interpretation reveals the key multilevel design rules governing the sensing response, establishing a generalizable framework that links bioinspired geometry, interfacial mechanics, and pressure-sensing behavior. This integrated structure-mechanism-modeling strategy provides a practical route toward next-generation ultrawide-range flexible sensors for wearable electronics and human-machine interfaces.

1 | Introduction

Flexible pressure sensors and electronic skin (e-skin) are increasingly recognized as enabling technologies for wearable health monitoring [1–5], artificial intelligence-assisted perception [6–10], and human-machine interfaces [11–14], owing to their ability to transduce mechanical stimuli into electrical signals with high sensitivity and spatial resolution [15–17]. In practical scenarios, these applications demand continuous and fine-grained pressure discrimination spanning an exceptionally wide range from subtle tactile stimuli [18] and physiological vibrations [19, 20] in the pascal regime to heavy mechanical loads [21] reaching the megapascal level. For example, plantar pressure during gait typically reaches ~0.3–1 MPa [22, 23], while dentistry [24], orthopaedics [25], and industrial robotics [26] frequently involve sustained MPa-level loading. Conversely, pulse signals and light touch [27, 28] generally occur below 10 kPa, imposing stringent requirements for high sensitivity at low pressures while maintaining linearity, resolution, and stability under large preloads. Achieving flexible pressure sensing over an ultra-wide range from Pa to MPa

All rights reserved, including rights for text and data mining and training of artificial intelligence technologies or similar technologies.
© 2026 Wiley-VCH GmbH

within a single flexible device remains a central challenge for next-generation wearable and interactive systems.

Among various transduction mechanisms, capacitive pressure sensors (CPSs) have been widely adopted due to their simple architecture, low power consumption, and favorable linear and dynamic response characteristics [29, 30]. A typical flexible CPS consists of two electrodes sandwiching a soft dielectric layer, with capacitance approximately described by $C \approx \varepsilon A/d$, where ε is the dielectric constant, A is the effective contact area between the electrodes and dielectric, and d is the distance between the two electrodes. However, conventional elastomeric dielectrics are nearly incompressible, leading to limited capacitance variation under applied pressure, sluggish response, and low sensitivity [31, 32]. To address this, extensive efforts have focused on introducing microstructured dielectric layers-such as microcolumns [33, 34], pyramids [35], domes [36], and porous architecture [37, 38] to enhance compressibility and sensitivity. While these designs significantly improve low-pressure performance, they commonly suffer from rapid structural hardening and capacitive saturation under medium-to-high pressures, restricting the linear operating range typically to below ~300 kPa [29, 32, 39, 40].

Iontronic capacitive sensors further amplify sensitivity by incorporating ionic dielectrics, where electric double layers (EDLs) form at the electrode/ionogel interface [41–43]. In such systems, the total capacitance is dominated by the unit-area capacitance of the EDL and the effective contact area, rendering pressure-induced contact evolution a critical determinant of sensor response. Iontronic strategies have enabled notable gains in sensitivity and detection limit; however, most reported devices remain confined to low-to-medium pressure regimes (≤400 kPa) [44–47]. Bio-templated and hierarchical microstructures inspired by natural surfaces have also been explored to enrich interfacial complexity, yet their inherent geometric randomness often leads to poorly controlled deformation pathways, limited linearity, and compromised reproducibility and manufacturability [28, 48]. Even recent graded [49] or programmable microstructuring [50] approaches, although extending detection ranges toward the MPa regime, still exhibit sensitivity roll-off, linearity collapse, or instability under high preloads (≥500 kPa), underscoring a persistent trade-off between sensitivity, linear range, and mechanical robustness.

These limitations collectively highlight the need for quantitatively programmable micro-architectures whose compressive behavior and contact-area evolution can be accurately predicted and rationally optimized. Such a design paradigm would enable sustained high sensitivity, broad linearity, and structural stability under deep compression, thereby providing a computable foundation for Pa to MPa pressure sensing rather than empirical trial-and-error optimization.

Here, we present a daisy-inspired gradient hemispherical array (GHA) iontronic pressure sensor enabled by an integrated structure-mechanism-modeling strategy. The device incorporates multilevel hemispherical units arranged in a top-down gradient configuration, in which the geometry, size, and spacing are synergistically optimized under finite-element guidance to programmably regulate structural compressibility and contact-area evolution under external loading. To further generalize and interpret these mechanics-guided insights, we establish a simulation-trained surrogate model combined with Shapley-value analysis, which quantitatively captures the structure-response relationship and corroborates the governing design rules across the explored parameter space. This combined strategy effectively suppresses capacitive saturation under high preloads and extends the sensing range across the full Pa-MPa regime.

As a result, the optimized device exhibits consistently high sensitivity exceeding 122 kPa^{-1} over 0–2555 kPa and delivers an ultrahigh sensitivity of 1864 kPa^{-1} in the low-pressure regime (0–61 kPa) with a wide linear response. The synergy between the graded microstructure array and the enhanced iontronic interfacial field further enables a low detection limit, high-pressure resolution at MPa-level loading, and stable operation over more than 5700 cycles under sustained high-pressure. Collectively, this work establishes a predictive and generalizable design framework for ultra-wide range, high-precision pressure sensing, with broad relevance to wearable electronics, robotics, medical monitoring, and extreme-environment applications.

2 | Results

2.1 | Design and Formation of GHA

Achieving ultra-wide-range flexible pressure sensing across multiple orders of magnitude, from Pa to MPa, remains a central challenge in this field, because the device must simultaneously satisfy two inherently competing requirements: sufficient deformability under weak stimuli to enable rapid triggering and high sensitivity, and sufficient structural stability under large loads to sustain continuous output while retaining the ability to resolve subtle pressure variations and avoid premature failure. As illustrated in Figure 1a, attaining such cross-scale pressure detection is a key objective for next-generation flexible pressure sensors. However, most existing designs still struggle to simultaneously deliver high sensitivity, a wide sensing range, and stable signal evolution over the entire loading regime.

As shown in Figure 1b, conventional microstructured pressure sensors generally employ single-scale structural units, such as hemispheres, cones, and pillars, to modulate local deformation and interfacial contact. These compliant microstructures can undergo pronounced deformation under low pressure, rapidly establish interfacial contact, and therefore typically exhibit high initial sensitivity. However, as the applied pressure increases, their limited deformation space is quickly exhausted, while the relatively simple local stress distribution leads to structural densification, restricted contact-area evolution, and premature signal saturation, resulting in a marked decline in response. Consequently, conventional single-scale architectures are inherently limited in their ability to effectively decouple low-pressure sensitivity from high-pressure load-bearing capability, which fundamentally underlies the long-standing difficulty in simultaneously achieving high sensitivity and a wide sensing range.

For iontronic flexible pressure sensors, enhancing the compressibility of the ionogel microstructure facilitates more pronounced effective contact-area evolution under each incremental pressure input, thereby delaying response saturation in the high-pressure

16163028, 2026, 71, Downloaded from https://advanced.onlinelibrary.wiley.com/doi/10.1002/adfm.77497 by Beihang University (Buaa), Wiley Online Library on [23/09/2026]. See the Terms and Conditions (https://onlinelibrary.wiley.com/terms-and-conditions) on Wiley Online Library for rules of use; OA articles are governed by the applicable Creative Commons License

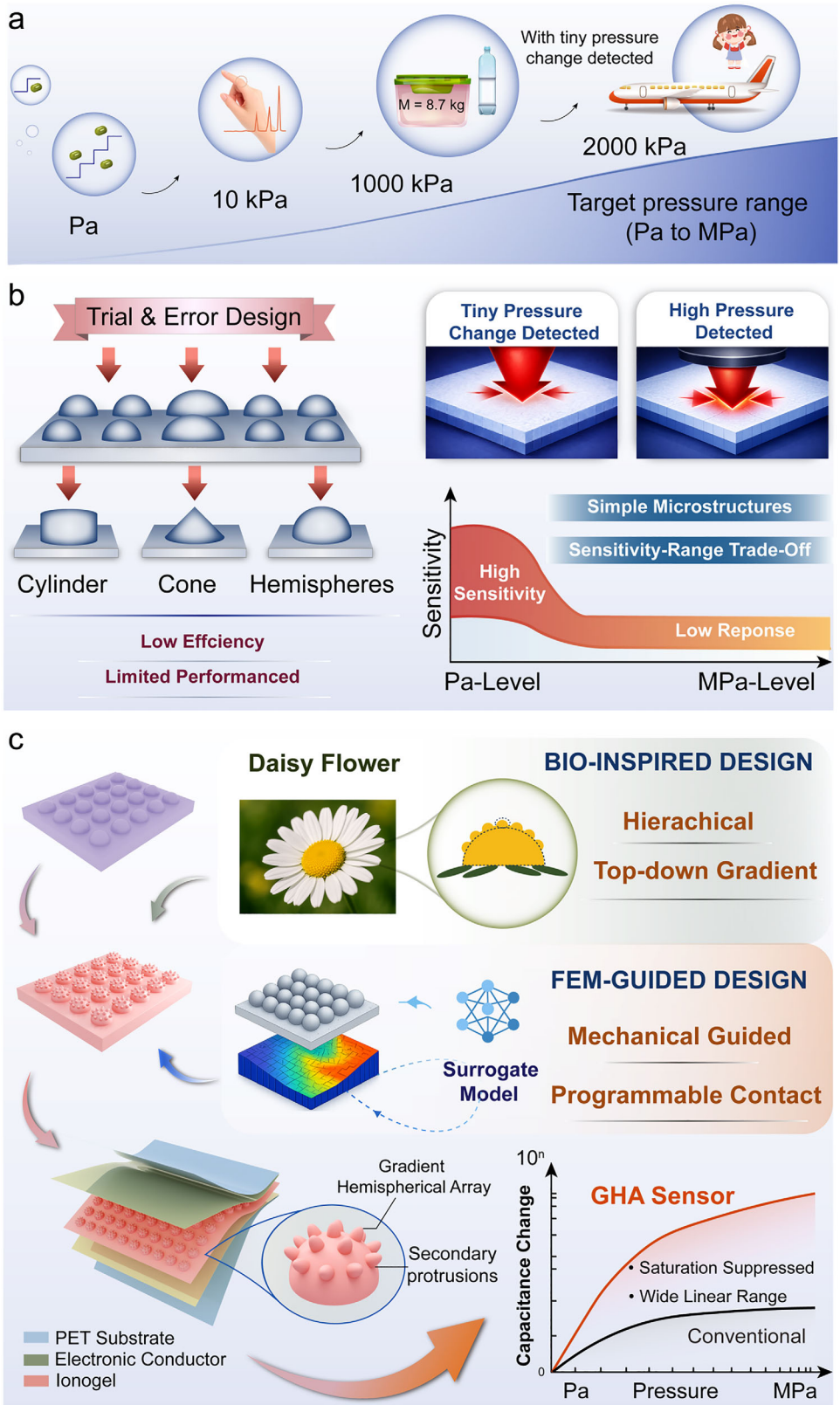

FIGURE 1 | Bioinspired Gradient Hemispherical Array (GHA) Iontronic Pressure Sensor: Design Concept and Mechanics. (a) Key objective and central challenge in ultrabroad-range flexible pressure sensing. (b) Intrinsic trade-off between sensitivity and sensing range in conventional single-scale microstructures. (c) Structural design and mechanics-regulated sensing of the bioinspired gradient hemispherical array.

16163028, 2026, 71, Downloaded from https://advanced.onlinelibrary.wiley.com/doi/10.1002/adfm.77497 by Beihang University (Buaa), Wiley Online Library on [23/09/2026]. See the Terms and Conditions (https://onlinelibrary.wiley.com/terms-and-conditions) on Wiley Online Library for rules of use; OA articles are governed by the applicable Creative Commons License

regime and improving operational stability [51, 52]. Guided by this design rationale, we developed a bioinspired gradient hemispherical array (GHA) iontronic pressure sensor and proposed an integrated structure–mechanism–modeling strategy. As illustrated in Figure 1c, the device is composed of multilevel hemispherical units arranged in a top-down gradient configuration, with its architecture inspired by the hierarchical and densely packed natural organization of the daisy capitulum. This bioinspired geometric structure provides a structural basis for orderly load sharing and sequential contact formation during compression [53, 54]. Under the guidance of finite-element simulations, we synergistically optimized the geometry, size, and spacing of the GHA to regulate structural compressibility and contact-area evolution. In parallel, a simulation-trained surrogate model combined with Shapley-value analysis was employed to generalize the structure–response relationship and extract the governing design rules. Compared with conventional microstructures, the resulting multilevel mechanics-regulated strategy effectively suppresses capacitive saturation under high preloads, thereby enabling stable pressure sensing over an ultra-wide range from Pa to MPa.

2.2 | Optimize Design and Characterizations of the GHA Architecture

For iontronic pressure sensors, the sensing signal originates from the electric double layer (EDL) formed at the electrode/ionogel interface. When external pressure P is applied, the interfacial microstructure deforms, increasing the contact area A and thereby raising the EDL capacitance (Figure 5e). According to the classical Gouy-Chapman-Stern (GCS) model, the EDL comprises a compact Helmholtz layer and a diffusion layer, with corresponding capacitances C_H and C_D. The total EDL capacitance can be expressed as [55, 56]

$$C_{EDL} = \left(\frac{1}{C_H} + \frac{1}{C_D}\right)^{-1} = \eta_A \cdot \varphi\,(d_H, \varepsilon, \sigma, T) \cdot A = UAC \cdot A \quad (1)$$

where η_A denotes the roughness factor, $\varphi(d_H, \varepsilon, \sigma, T)$ is the unit-area capacitance determined by the Helmholtz-layer thickness d_H, electrolyte dielectric constant ε, ionic conductivity σ, and ambient temperature T. For a given material system, UAC (i.e., η_A φ) can be approximately as constant, leaving the effective contact area A as the principal variable under compression. Hence, the slope of the A-P curve and the high linear range determine sensitivity and operating range, respectively (see Section S1 for detailed derivation).

To elucidate the mechanical basis by which the GHA sustains continuous interfacial response over a broad pressure range, we first performed finite-element analysis (FEA) to systematically compare different single-layer microstructures. Four representative microgeometries-cylindrical, conical, pyramidal, and hemispherical-were simulated (Figure 2a) to assess their stress-strain distribution and contact-area evolution under compression. In capacitive pressure sensors based on the electric double layer (EDL) mechanism, the normalized signal variation predominantly arises from changes in the relative contact area ($\Delta A/A_0$) at the electrode-dielectric interface, which are governed by the compressibility of the microstructure. As shown in Figure 2b,c, the cylindrical structure rapidly achieves full contact and exhibits near-incompressibility, so the contact area increases only slightly with increasing pressure. Conical and pyramidal structures exhibit small initial contact areas, enabling high initial sensitivity at low pressures. However, as pressure increases, the pronounced stress concentration at their sharp tips accelerates structural compaction, which may reduce the subsequent contact-area increment and lead to sensitivity degradation or response saturation [35, 57]. In contrast, hemispherical structures feature continuous curvature and a more uniform stress distribution, allowing the contact region to expand progressively and maintain a sustained response over a broader pressure range [45, 58]. As shown in Figure S1, the pyramid-structured sensor shows a comparable or slightly higher initial response below 100 kPa due to tip-induced stress concentration, but its response growth becomes limited at higher pressures. In contrast, the hemispherical sensor exhibits higher overall sensitivity over a similar detection range: 48.06 kPa^{-1} over 0–536 kPa, compared with 31.52 kPa^{-1} over 0–535 kPa for the pyramid-structured sensor, supporting its selection as the basic unit for the hierarchical gradient design. Linear fitting further confirmed the higher overall sensitivity of the hemispherical device, supporting its selection as the basic unit for the subsequent hierarchical gradient design.

On this basis, we constructed the GHA and analyzed its staged deformation and contact evolution during platen loading (Figure 2d). Rather than undergoing synchronous bulk compression, the GHA exhibits a distinct sequential-contact behavior. Taking GHA with h/d = 1 as a representative case (corresponding to Figure 2fiii), the upper small hemispheres first engage the electrode at low pressure, driving rapid growth of the effective contact area. With increasing load, the middle and lower layers are progressively recruited, redistributing stress while sustaining continuous contact-area growth; at high-pressure, further deformation of the bottom hemispheres continues to dissipate local stress and delay saturation (Figure 2e). This staged compression behavior alleviates local stress concentration and promotes cooperative evolution across multiple interfaces, thereby transforming a rapidly saturating single-stage response into a sustained multistage output. The key advantage of the GHA therefore lies not merely in enhanced instantaneous interfacial response, but in its ability to deliver more controllable contact-area evolution and a more stable mechanical response through hierarchical structural design.

Further, the gradient geometric parameters of the GHA were systematically optimized, as summarized in Figure 2f (i) We first screened three architectures, namely the cylindrical-base hierarchical array (Cyl-HA), conical-base hemispherical array (Cone-HA), and the GHA. Compared with the former two, the GHA exhibited a smoother and more continuous $\Delta A/A_0$–pressure evolution across different interfaces, together with a larger $\Delta A/A_0$ variation range, indicating a more favorable staged-contact process and a more nearly linear sustained response (Figure S2). (ii) We then tuned the polar angle of the second-layer micro-hemispheres (θ = 35°, 50°, and 65°). Varying θ changes the spatial distribution, contact-point density, and local curvature of the second-layer units, thereby modulating the growth rate of $\Delta A/A_0$ and the linear operating range. Among the tested configurations, θ = 50° yielded the most uniform contact-area

16163028, 2026, 71, Downloaded from https://advanced.onlinelibrary.wiley.com/doi/10.1002/adfm.77497 by Beihang University (Buaa), Wiley Online Library on [23/09/2026]. See the Terms and Conditions (https://onlinelibrary.wiley.com/terms-and-conditions) on Wiley Online Library for rules of use; OA articles are governed by the applicable Creative Commons License

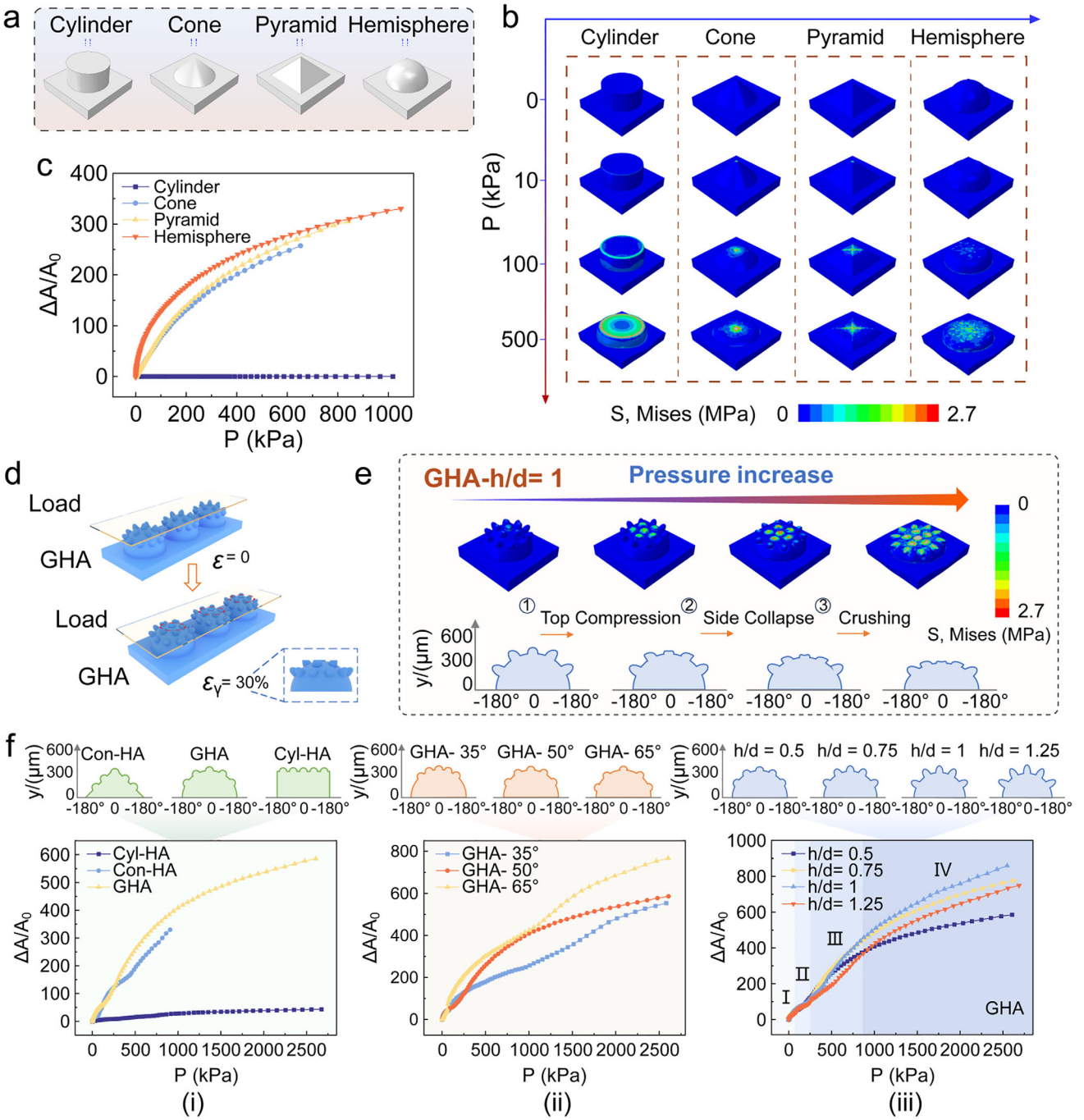

FIGURE 2 | Optimized design and characterization of the GHA structure. (a) Schematics of four single-layer microstructures, including cylindrical, conical, pyramidal, and hemispherical geometries. Finite-element analysis (FEA) showing (b) stress distributions under compression and (c) the change in normalized real contact area $\Delta A/A_0$ at the electrode-ionic interface for the different microstructures. (d) Schematic illustration of the deformation mechanism of the GHA during platen loading. (e) Finite-element simulated staged deformation behavior of the GHA with h/d = 1 under compression, corresponding to (fiii). (f) Effects of gradient geometric modulation on hierarchical contact-area growth, including (i) structural screening (Cyl-HA, Con-HA, and GHA), (ii) the polar angle of the second layer (θ), and (iii) different aspect ratios (h/d) of the second layer; the corresponding $\Delta A/A_0$–pressure relationships at different interfaces are shown.

growth. (iii) Finally, based on the GHA-50° structure, the aspect ratio (h/d) of the second-layer micro-hemispheres was further optimized. Within the investigated design space, the GHA with h/d = 1 exhibited a more stable deformation mode, smoother contact-area evolution, and reduced stress concentration relative to the other tested configurations, suggesting improved mechanical robustness. These results demonstrate that rational gradient geometric regulation can simultaneously enhance structural compressibility and the uniformity of contact-area evolution, thereby providing a key design principle for achieving highly sensitive pressure sensing over a broad linear operating range.

16163028, 2026, 71, Downloaded from https://advanced.onlinelibrary.wiley.com/doi/10.1002/adfm.77497 by Beihang University (Buaa), Wiley Online Library on [23/09/2026]. See the Terms and Conditions (https://onlinelibrary.wiley.com/terms-and-conditions) on Wiley Online Library for rules of use; OA articles are governed by the applicable Creative Commons License

2.3 | Data-Driven Surrogate Modeling for Interpretable Microstructure Design

To accelerate microstructure optimization and extract interpretable design rules from the finite-element dataset, a machine-learning-assisted surrogate framework was established. Conventional finite-element analysis is usually limited to point-by-point evaluation of a finite number of structural combinations, making it difficult to systematically quantify the relative contribution of different geometric parameters. The surrogate model converts these simulation results into quantitative and interpretable design rules, thereby guiding subsequent microstructure-parameter optimization. As shown in Figure 3a, a simulation-derived geometry–loading dataset was constructed to train and benchmark multiple tree-based regressors for the nonlinear structure–response relationship between structural descriptors and FEA-derived mechanical/contact responses. Extra Trees (ET) delivered the lowest prediction error, with a root mean square error (RMSE) of ≈2.7 and a mean absolute percentage error (MAPE) of ≈1.7%, both markedly lower than those of Random Forest (RF), Gradient Boosting (GB), and Extreme Gradient Boosting (XGB) (Figure 3b). The optimized ET model showed excellent predictive accuracy over the entire response range, with the predicted values almost perfectly overlapping the true values along the ideal y = x line (R^2 = 0.9998, Figure 3c). These results indicate that the surrogate model can accurately approximate the finite-element-derived input–output mapping and serve as an efficient screening tool within the predefined design space, rather than a complete replacement for FEA or experiments.

On this basis, descriptor-importance and Shapley additive explanations (SHAP) analyses were further performed to identify the key parameters governing the structural response. Pressure was the dominant predictor, followed by geometric morphology, whereas angle, small-HA size, and small-HA height showed secondary but non-negligible contributions (Figure 3d). Since pressure is an externally applied loading parameter rather than a tunable geometric descriptor, it was excluded from Figure 3e to better resolve the geometry-dependent effects. Within this geometry-centered framework, Cyl-HA was mainly associated with negative SHAP values, whereas GHA showed predominantly positive contributions, indicating distinct roles of large-scale morphology in modulating the predicted response. Among the small-scale geometric states, GHA with h/d = 1 emerged as the most favorable configuration within the present design space, while GHA with h/d = 0.5 and GHA with h/d = 1.25 tended to contribute negatively. By contrast, GHA with h/d = 0.75, small-HA height, and Con-HA remained largely centered around zero, suggesting relatively limited effects within the present design space. Collectively, these results show that the FEA-derived mechanical and contact response is governed by a limited set of geometry-sensitive descriptors that regulate stress redistribution and contact evolution. Therefore, the surrogate framework provides quantitative guidance for identifying key structural parameters and supports the optimization of the GHA architecture.

2.4 | Fabrication and Characterization of the Ionogel

Guided by finite element analysis (FEA), we selected a graded hemispherical array with a second-stage polar angle of 50° (GHA-50°) and a second-stage height-to-diameter ratio h/d = 1 for fabrication. The array was realized using high-precision printing equipment to generate a structured master, which was replicated into a polydimethylsiloxane (PDMS) negative mould. In Figure 4a, we used PVA/H_3PO_4 ionogel as the dielectric layer and patterned it via a PDMS-membrane-assisted casting/spin-coating process. In this process, we deposited the ionogel precursor onto the structured PDMS negative, then cured and demoulded it to obtain a uniform GHA ionogel membrane (see Methods for details).

At the microscopic level, Figure 4b (i) and Figure S3 present three-dimensional optical topography and surface profilometry of the microstructure, revealing high replication fidelity and uniform morphology that closely matches the designed pattern. Figure 4b (ii, iii) shows top-view and cross-sectional SEM images of the PDMS negative and the ionogel film, confirming accurate transfer of the GHA geometry with uniform feature height and pitch across the entire field. Figure 4c,d further display a macroscopic photograph and topographic map of the structured ionogel, demonstrating an orderly microstructure array with well-defined morphology. Finally, gold-plated polyethylene terephthalate (PET) films were employed as the top and bottom electrodes. It is worth noting that during sensor assembly, plasma treatment was used to improve substrate wettability and promote conformal contact between the ionogel film and the substrate [59]. As shown in Figure S4, the decreased contact angle after treatment confirms the improved wettability, which helps reduce interfacial gaps, edge warping, and delamination during testing. Detailed fabrication procedures are outlined in the Methods section.

2.5 | Sensing Performance of Iontronic Sensors with the Optimized GHA Architecture

Sensitivity, signal linearity, and sensing range serve as core metrics for evaluating its response performance. The sensor response is quantified by the normalized capacitance change $\Delta C/C_0$, where C and C_0 are the instantaneous and initial capacitances, respectively. The sensitivity is defined as

$$S = \frac{\Delta C/C_0}{\Delta P} \tag{2}$$

where C_0 is the initial capacitance before loading, ΔC is the corresponding change capacitance after pressure change (ΔP). When minute variations in pressure amplitude induce significant changes in capacitance, high sensitivity can be achieved. Prior to applying pressure, the initial capacitance is controlled within a few picofarads (pF) to account for potential microscopic air gaps in the microstructured ion layer and electrode layer [49, 60]. As shown in Figure 5a-c, the device exhibits a

16163028, 2026, 71, Downloaded from https://advanced.onlinelibrary.wiley.com/doi/10.1002/adfm.77497 by Beihang University (Buaa), Wiley Online Library on [23/09/2026]. See the Terms and Conditions (https://onlinelibrary.wiley.com/terms-and-conditions) on Wiley Online Library for rules of use; OA articles are governed by the applicable Creative Commons License

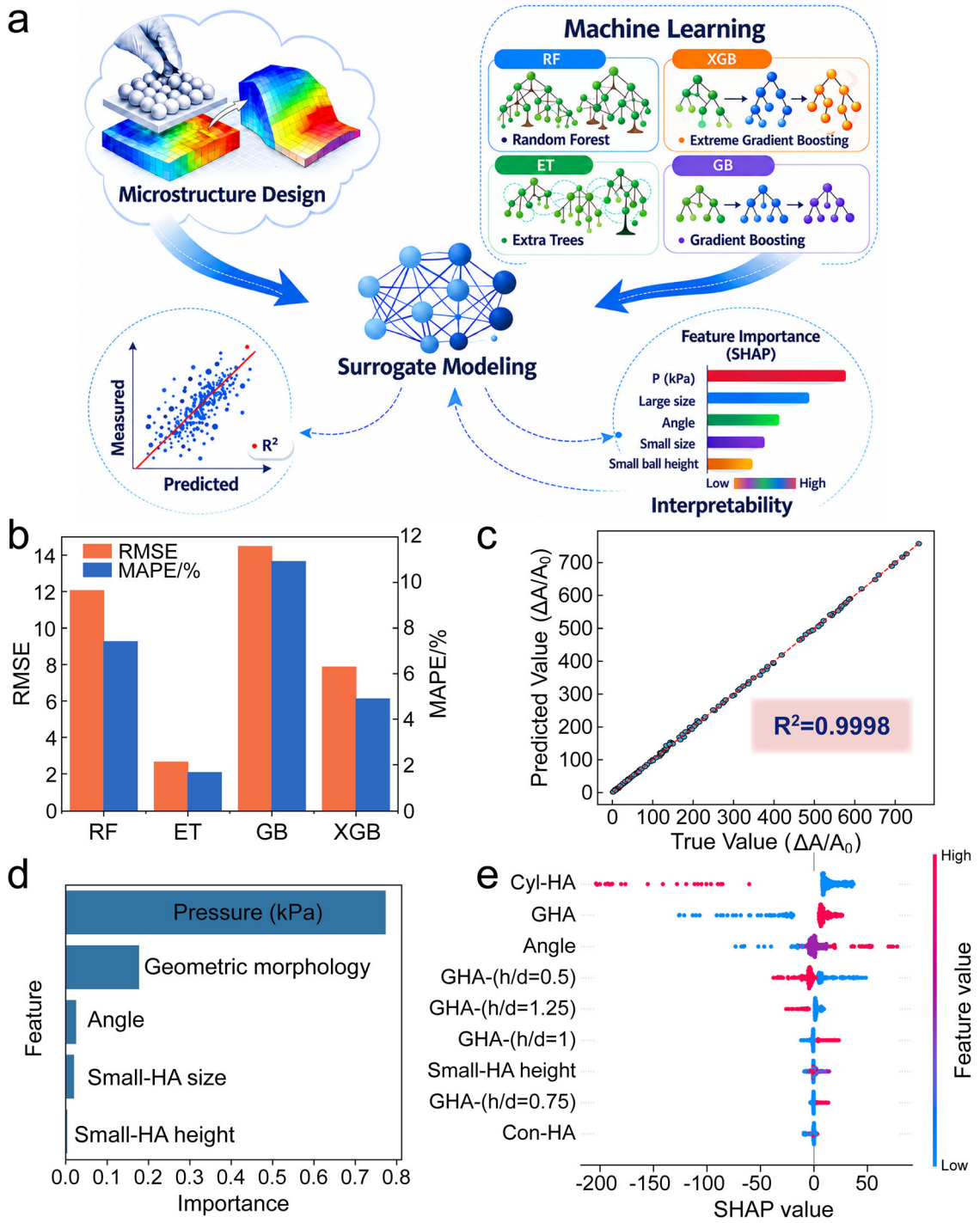

FIGURE 3 | Surrogate modeling and descriptor attribution for interpretable microstructure design. (a) Schematic illustration of the workflow for a machine learning-assisted agent framework model. (b) Performance comparison of Random Forest (RF), Extra Trees (ET), Gradient Boosting (GB), and Extreme Gradient Boosting (XGB) models in terms of root mean square error (RMSE) and mean absolute percentage error (MAPE). (c) Parity plot comparing the predicted and true values of the ET model. (d) Global importance ranking of the loading and geometric descriptors. (e) SHAP (Shapley additive explanations) beeswarm plot showing the magnitude and direction of the geometric descriptor contributions to the model output.

remarkably linear "step" response across three pressure ranges: low (~34.25-53.06 kPa), medium (~107-288 kPa), and high (~287.66-469.05 kPa). The response peak increases almost linearly with pressure, maintaining excellent linearity and stability across the full measurement range. As shown in Figure 5d, compared to the HA structure, the optimized GHA structure sensor maintains a sensitivity exceeding 122 kPa^{-1} over an ultra-wide detection range (up to 2555 kPa) while sustaining several broad quasi-linear response regimes. In the low-pressure regime (<61 kPa), the device exhibits an ultra-high sensitivity of S_1 = 1864.19 kPa^{-1} with a linearity as high as R_12 = 0.9993. In the medium-pressure range (61-283 kPa), the sensor remains highly sensitive (S_2 = 1581.71 kPa^{-1}) with R_2^2 = 0.996. In the high-pressure domain (283–881 kPa), it achieves S_3 = 468.05 kPa^{-1}, R_32 = 0.966.

16163028, 2026, 71, Downloaded from https://advanced.onlinelibrary.wiley.com/doi/10.1002/adfm.77497 by Beihang University (Buaa), Wiley Online Library on [23/09/2026]. See the Terms and Conditions (https://onlinelibrary.wiley.com/terms-and-conditions) on Wiley Online Library for rules of use; OA articles are governed by the applicable Creative Commons License

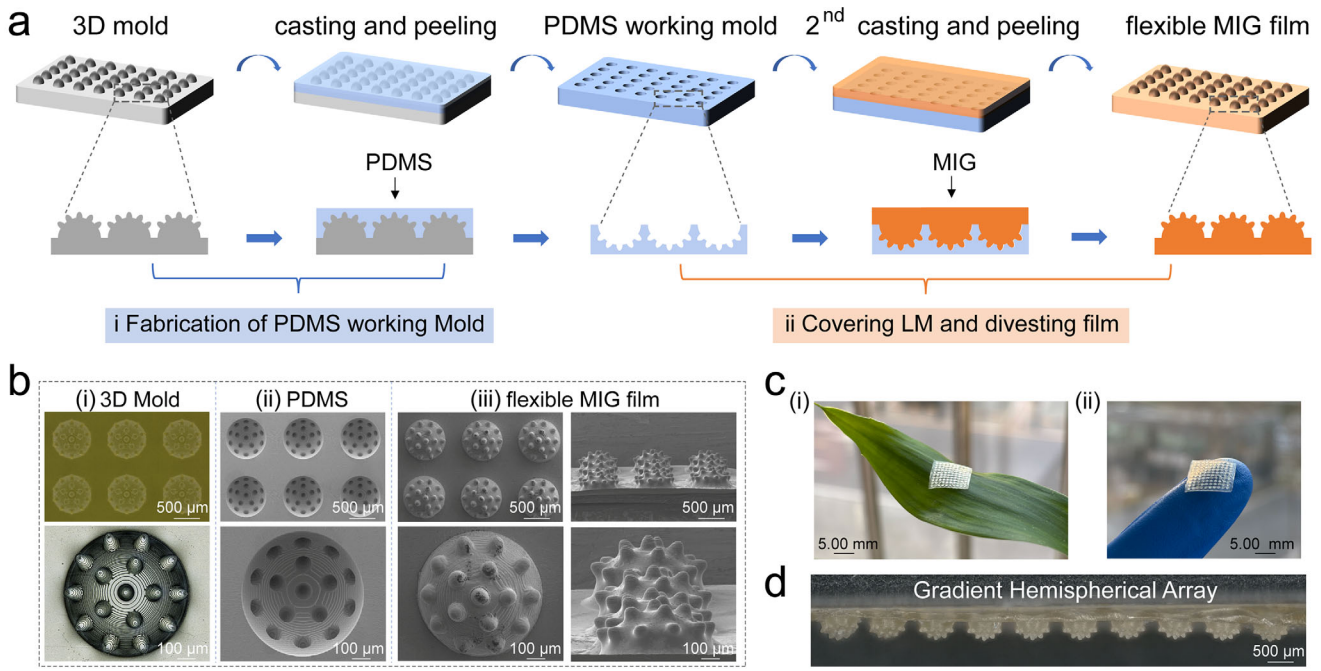

FIGURE 4 | Fabrication and structural characterization of GHA-patterned ionogel. (a) Schematic illustration of the template-assisted patterning strategy used to construct GHA-based ionogel dielectric layers. (b) Optical and SEM images: (i) 3D-printed mould (top-view optical image); (ii) PDMS negative mould (top-view SEM image); and (iii) morphological characterization of the GHA-structured ionogel in top- and cross-sectional SEM views. (c) Photograph of the fabricated GHA-patterned ionogel. (d) Three-dimensional optical microscopy image of the structured ionogel, illustrating the ordered microstructure array.

Crucially, even under ultra-high pressure (>881 kPa), the sensor exhibits near-linear high-sensitivity response ($R_4 2 = 0.967$) with $S_4 = 122.13\ \text{kPa}^{-1}$, extending its sensing range up to 2555 kPa. These results demonstrate that our GHA-patterned iontronic sensor achieves a rare combination of ultra-high sensitivity, exceptional linearity and ultra-wide sensing range, positioning it among the highest-performing pressure sensors reported to date.

Compared with conventional capacitive sensors, our iontronic pressure sensor exploits a fundamentally different sensing mechanism. As shown in Figure 5e, the ionogel contains a high concentration of mobile cations and anions. Under bias, electronic charge on the electrodes is balanced by counterions in the gel at the electrode-gel interface, forming nanoscale electric double layers (EDLs). Unlike conventional capacitors, the contact area of these EDL interfaces varies with applied pressure. In our device, the EDL capacitances at the patterned top interface ($C_{\text{EDL, top}}$) and the flat bottom interface ($C_{\text{EDL, bottom}}$) are connected as two interface capacitors in series with the bulk resistance (R_S) and in parallel with the coupling capacitance (C_E) between the electrodes, as shown in Figure S5. The total measured capacitance can thus be written as:

$$C = C_E + \frac{C_{\text{EDL,top}} C_{\text{EDL,bottom}}}{C_{\text{EDL,top}} + C_{\text{EDL,bottom}}} \tag{3}$$

Here, the bottom interface is in full contact and produces a large, constant $C_{\text{EDL, bottom}}$. The patterned top interface consists of many independent EDL elements C^n_{EDL}, so $C_{\text{EDL,top}} = \sum_n C^n_{\text{EDL}}$.

Because C_E is much smaller than either EDL capacitance and can be neglected. Therefore, the measured capacitance C is approximately equal to $C_{\text{EDL, top}}$.

To elucidate why the GHA architecture sustains both high sensitivity and linearity over a wide pressure range, we partitioned the response into four physical stages via segmented linear regression of the $\Delta C/C_0$-P calibration curve, supported by FEA and microstructural morphology (Figure 5f). In Stage I (0-61 kPa), the top-tier hemispheres first contact the electrode and undergo primary deformation, rapidly increasing the EDL interface area A_{EDL}. This increase leads to a steep response slope and yields ultra-high initial sensitivity. Stage II (61–283 kPa) is characterized by sequential engagement of the secondary hemispheres, enabling multi-point load sharing and stress redistribution; the EDL contact area grows approximately in proportion to pressure, so the response slope remains nearly constant over this broad interval. In Stage III (283–881 kPa), the outer ring and base hemispheres compress together, micro-buckling appears on the surface micro-hemispheres, and new contact patches keep forming; the capacitance continues to rise steadily without premature saturation. Finally, in Stage IV (0.881–2.555 MPa) the surface micro-hemispheres flatten and conform fully to the substrate hemisphere; further compression is dominated by the substrate hemisphere, and A_{EDL} expands smoothly in the MPa range, thereby extending the upper detection limit. Overall, the hierarchical gradient hemispherical array activates a stepwise contact-propagation-area-scaling-stress-redistribution mechanism. This mechanism enables an ultra-wide segmented linear operating window while retaining high sensitivity.

16163028, 2026, 71, Downloaded from https://advanced.onlinelibrary.wiley.com/doi/10.1002/adfm.77497 by Beihang University (Buaa), Wiley Online Library on [23/09/2026]. See the Terms and Conditions (https://onlinelibrary.wiley.com/terms-and-conditions) on Wiley Online Library for rules of use; OA articles are governed by the applicable Creative Commons License

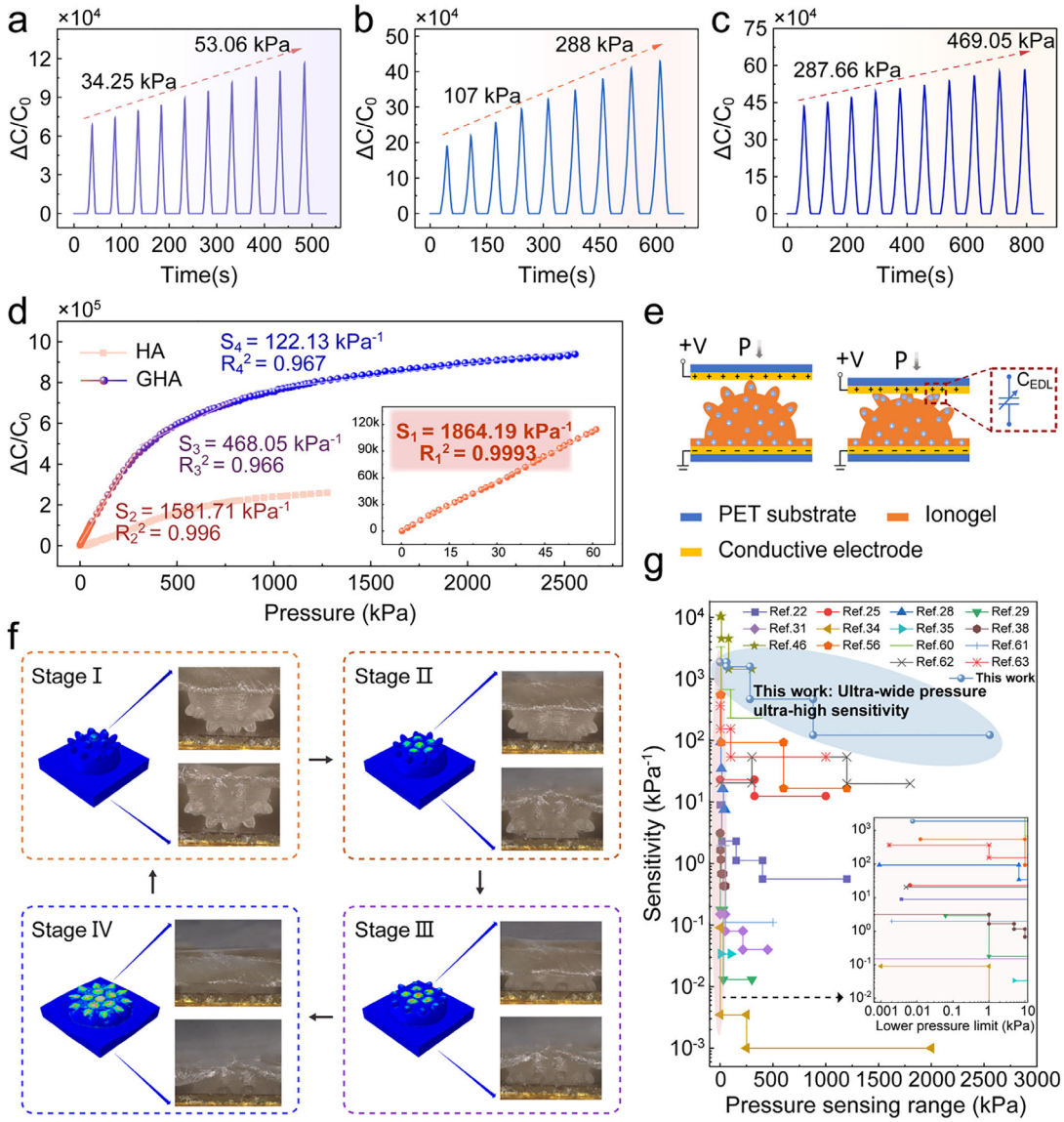

FIGURE 5 | Sensing performance and structural analysis of the GHA-based iontronic Pressure Sensor. (a–c) Real-time step-loading response under low- (34.25–53.06 kPa), medium- (107–288 kPa) and high-pressure (287.66–469.05 kPa) regimes. (d) Comparison of the capacitance–pressure response for devices with and without the GHA structure. (e) Schematic of the iontronic sensing mechanism, showing EDL formation and contact-area modulation under loading. (f) Finite-element analysis (FEA) of GHA deformation and evolution of the EDL interfacial contact area A_{EDL} across Stages I-IV. (g) Performance comparison between this work and other capacitive pressure sensors in terms of sensitivity and pressure detection range. The inset shows the corresponding limit of detection.

As shown in Figure S6, GHA-structured sensors fabricated from different batches exhibit good response consistency. The inset images show well-defined GHA morphologies in all three devices, indicating good structural reproducibility and device-to-device repeatability of the fabrication process. In parallel (Figure 5g), the sensor preserves a segmented, near-linear calibration across an ultra-wide pressure span while sustaining high sensitivity within each segment. Compared with conventional parallel-plate capacitive sensors and other EDL-based iontronic sensors [22, 25, 28, 29, 31, 34, 35, 38, 46, 56, 60–63], our device maintains a sensitivity exceeding 100 kPa^{-1} over the entire pressure range from the Pa to MPa regime, highlighting its synergistic combination of low-pressure detection capability, broad sensing range, and high sensitivity.

2.6 | Ultra-Wide Linear Dynamic Response

Most flexible pressure sensors are electrically characterized over only a narrow segment of their nominal sensing range [46, 50, 62]; by contrast, our device maintains highly linear and dynamically stable responses across the full ultrabroad operating window, enabling rigorous full-range benchmarking. We next challenged the GHA-structured pressure sensor with cyclic gradient and rate-dependent loading protocols to elucidate its ultrabroad linear dynamic response. As shown in Figure 6a, under cyclic step loading in the low-pressure regime (1.79–38.82 kPa), the device exhibits clearly resolved, step-like response levels whose amplitude increases monotonically with pressure, while the baseline fully recovers after each cycle, yielding a high signal-to-noise ratio

16163028, 2026, 71, Downloaded from https://advanced.onlinelibrary.wiley.com/doi/10.1002/adfm.77497 by Beihang University (Buaa), Wiley Online Library on [23/09/2026]. See the Terms and Conditions (https://onlinelibrary.wiley.com/terms-and-conditions) on Wiley Online Library for rules of use; OA articles are governed by the applicable Creative Commons License

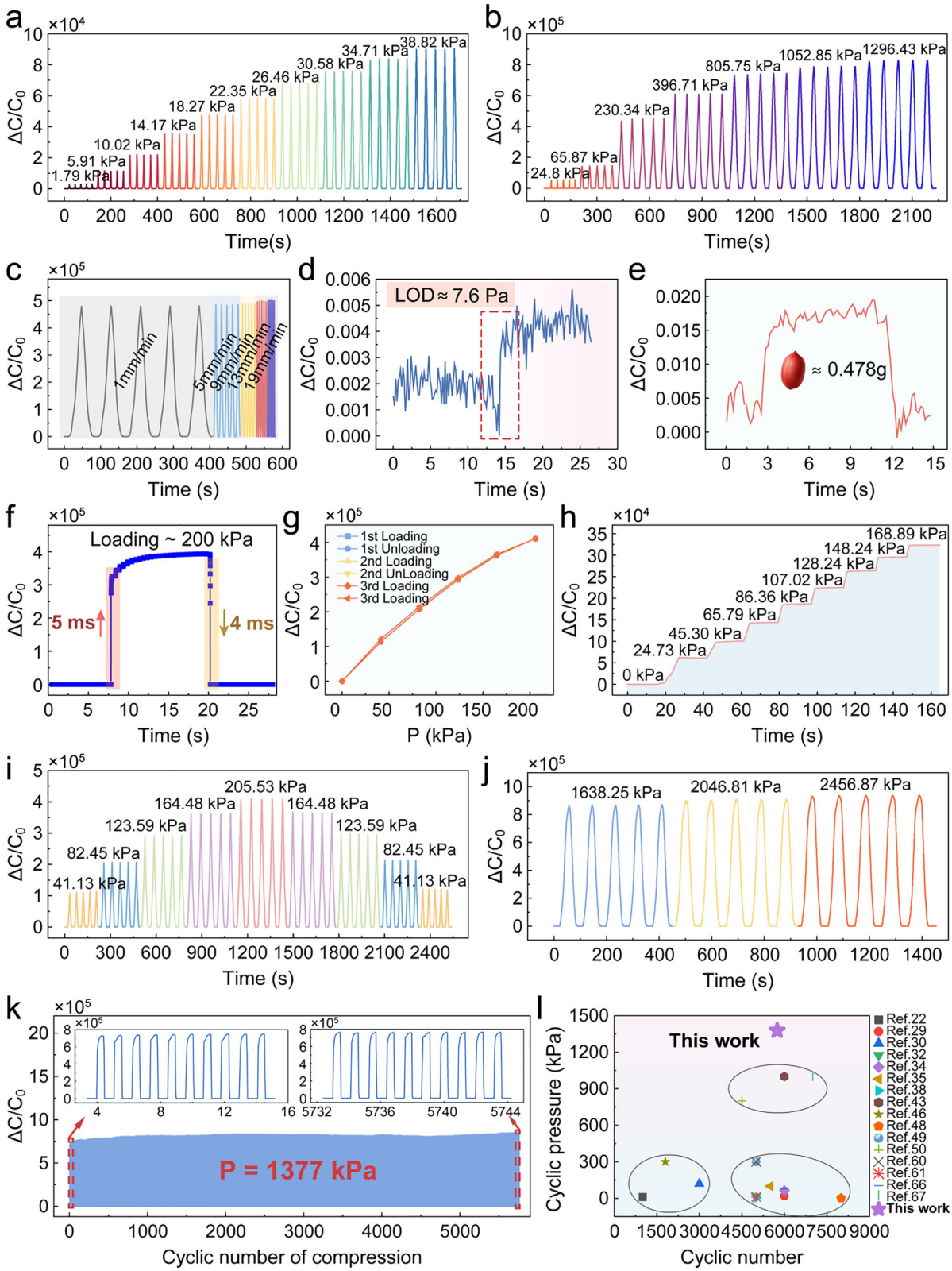

FIGURE 6 | Full-range dynamic pressure response. (a,b) Real-time capacitance responses under continuously ramped loading in low- (1.79–38.82 kPa) and wide- (24.8–1296.43 kPa) pressure ranges. (c) Dynamic responses at 227 kPa across different loading rates. (d) Verification of the detection limit (≈7.6 Pa) by loading a single mung bean. (e) Detection of micro-loads from individual peanut kernels. (f) Response and relaxation times of the device under 200 kPa loading. (g) Hysteresis characteristics over three loading (200 kPa) / unloading cycles. (h) Stability under stepwise pressure loading. (i) Stability under cyclic pressures between 41.13–205.53 kPa. (j) Dynamic capacitance responses under ultra-high pressures of 1638, 2047 and 2457 kPa. (k) High-pressure durability over 5700 loading-unloading cycles at 1377 kPa. (l) Reported cyclic pressure and cyclic number for this work and recently reported capacitive pressure sensors.

16163028, 2026, 71, Downloaded from https://advanced.onlinelibrary.wiley.com/doi/10.1002/adfm.77497 by Beihang University (Buaa), Wiley Online Library on [23/09/2026]. See the Terms and Conditions (https://onlinelibrary.wiley.com/terms-and-conditions) on Wiley Online Library for rules of use; OA articles are governed by the applicable Creative Commons License

and excellent resolution at low pressures. In Figure 6b, real-time cyclic loading over wide pressure levels (24.8, 65.87, 230.34, 396.71, 805.75, 1052.85 and 1296.43 kPa) produces stable, reversible and highly repeatable capacitance responses at each pressure point. The transitions during loading/unloading are rapid and well defined, with no observable drift or attenuation, and segmented linear regression confirms consistent sensitivity and linearity across the different pressure intervals. Furthermore, as shown in Figure 6c, under continuous loading at a target pressure of 227 kPa with loading rates of 1, 5, 9, 13 and 19 mm/min, the sensor delivers fast and repeatable responses for all rates. The output signals remain stable and free of noticeable attenuation, indicating a reliable correspondence between pressure input and capacitance readout and demonstrating robust multi-rate dynamic monitoring capability.

Moreover, our sensor demonstrates exceptional resolution even for minute loads. As shown in Figure 6d, e, we tested the device under minimal external loading conditions: placing mung beans (0.0776 g) and peanuts (0.478 g) on the sensor produced pressures of 7.6 and 46.8 Pa, respectively-and even at ≈7 Pa increments, the sensor generated a clear response. This indicates rapid, stable signals at pressures well below the ≈100 Pa detection threshold of human skin [31, 64]. Figure 6f further shows that under a cyclic loading/unloading condition of ≈200 kPa, the sensor achieves a response time of ≈5 ms and a relaxation time of ≈4 ms, which are far shorter than the 30–50 ms perceptual response time of human skin and superior to most flexible pressure sensors reported to date [22, 56]. Previous studies have shown that hysteresis may cause signal phase lag and dynamic measurement errors, thereby affecting measurement accuracy and practical reliability [14, 65]. After three consecutive loading/unloading cycles over the ≈200 kPa span (Figure 6g), the device displays good immediate repeatability and minimal hysteresis. Such low hysteresis behavior helps reduce response bias and signal delay, improving measurement reliability in continuous pressure monitoring and human–machine interaction.

To assess the sensor's stability and linear output behavior, we characterized its capacitive response under progressively increasing pressure. In Figure 6h, we applied step-wise loading at ≈20 kPa intervals over the 0–170 kPa range and observed clearly separated, monotonic step-like response levels with no overlap or drift between steps, demonstrating excellent stability and near-linear performance. Next (Figure 6i), we conducted loading/unloading sequences at 41.13, 82.45, 123.59, 164.48 and 205.53 kPa; the resulting response curves are linear, orderly and nearly mirror-symmetric, underscoring outstanding linearity, repeatability and operational stability. Together, these continuous, near-proportional step responses enable precise calibration and real-time monitoring in complex pressure environments.

2.7 | Robustness Under Complex Operating Conditions and High-Load Durability

We further evaluated the device performance under extreme high-pressure conditions. As shown in Figure 6j, the sensor maintains stable and well-resolved response signals under ultra-wide pressures from 1.638 to 2457 kPa. Despite such severe mechanical deformation, no structural instability or functional degradation is observed, evidencing excellent mechanical robustness and signal stability. Furthermore, mechanical durability under high loads is crucial for the long-term stable operation of devices in complex working conditions. However, existing literature on cyclic testing methods still lacks unified standards regarding pressure amplitude and cycle count. Good mechanical stability is essential for the long-term reliable operation of flexible pressure sensors. Figure 6k shows that the device maintained a stable response after more than 5700 loading/unloading cycles at 1377 kPa, with no noticeable signal drift, indicating good cyclic durability under this testing condition. As shown in Figure 6l and Table S1, we further summarized representative flexible pressure sensors in terms of sensing type, structural design, sensitivity, sensing range, cyclic testing pressure, and cycle number for reference. In parallel, the sensor preserves stable sensing performance across its exceptionally broad detection range and compares favorably with most reported devices [22, 29, 30, 32, 34, 35, 38, 43, 46, 48–50, 60, 61, 66, 67] (Figure 6l).

Stable responses over different time scales and under environmental disturbances are essential for reliable pressure monitoring. As shown in Figure S7, the same device maintains stable and repeatable dynamic responses under ≈100 kPa on days 1, 7, and 14, with no obvious signal attenuation or drift. In addition, as shown in Figure S8, the device exhibits stable responses over 26°C–47°C and retains 90.13% of its response when the relative humidity increases from 40% RH to 70% RH, while maintaining clearly distinguishable loading/unloading signals. Stable responses are also preserved under different bending states (Figure S9), demonstrating good reliability under complex operating conditions. Collectively, these results indicate that the GHA-structured sensor maintains stable and reliable sensing performance under high-pressure loading, long-term use, environmental disturbances, and mechanical deformation, highlighting its practical potential for complex operating conditions.

2.8 | Extremely High-Pressure Resolution

A salient feature of our GHA-based iontronic pressure sensor is its combination of high sensitivity across a broad pressure range and the capability to resolve minute perturbations even under high-pressure preloads, thereby enabling cross-scale pressure monitoring. By contrast, many flexible pressure sensors exhibit response slowdown or saturation at several hundred kilopascals, with typical upper limits around 0.4-1 MPa [22, 63, 65, 68], which severely restricts high-pressure resolution and the detection of subtle pressure fluctuations under heavy loads. High-resolution sensing in the MPa regime is therefore particularly critical. Figure 7a schematically illustrates the dual-response mode of our device: it responds to low-pressure stimuli while simultaneously resolving small pressure disturbances superimposed on high-pressure states, reflecting its broad adaptability for multi-scale pressure monitoring. For sensors prone to saturation or reduced sensitivity at high pressures, stable resolution of small additional pressure changes under large preloads remains challenging. To quantitatively assess its resolution under ultra-high pressure, we applied four incremental 15 kPa steps at reference pressures of 0, 1000, 1500 and 2000 kPa. The overall (bottom) and magnified (top) response curves are shown in Figure 7b–e. Across all reference pressures, each 15 kPa increment induces a clear,

16163028, 2026, 71, Downloaded from https://advanced.onlinelibrary.wiley.com/doi/10.1002/adfm.77497 by Beihang University (Buaa), Wiley Online Library on [23/09/2026]. See the Terms and Conditions (https://onlinelibrary.wiley.com/terms-and-conditions) on Wiley Online Library for rules of use; OA articles are governed by the applicable Creative Commons License

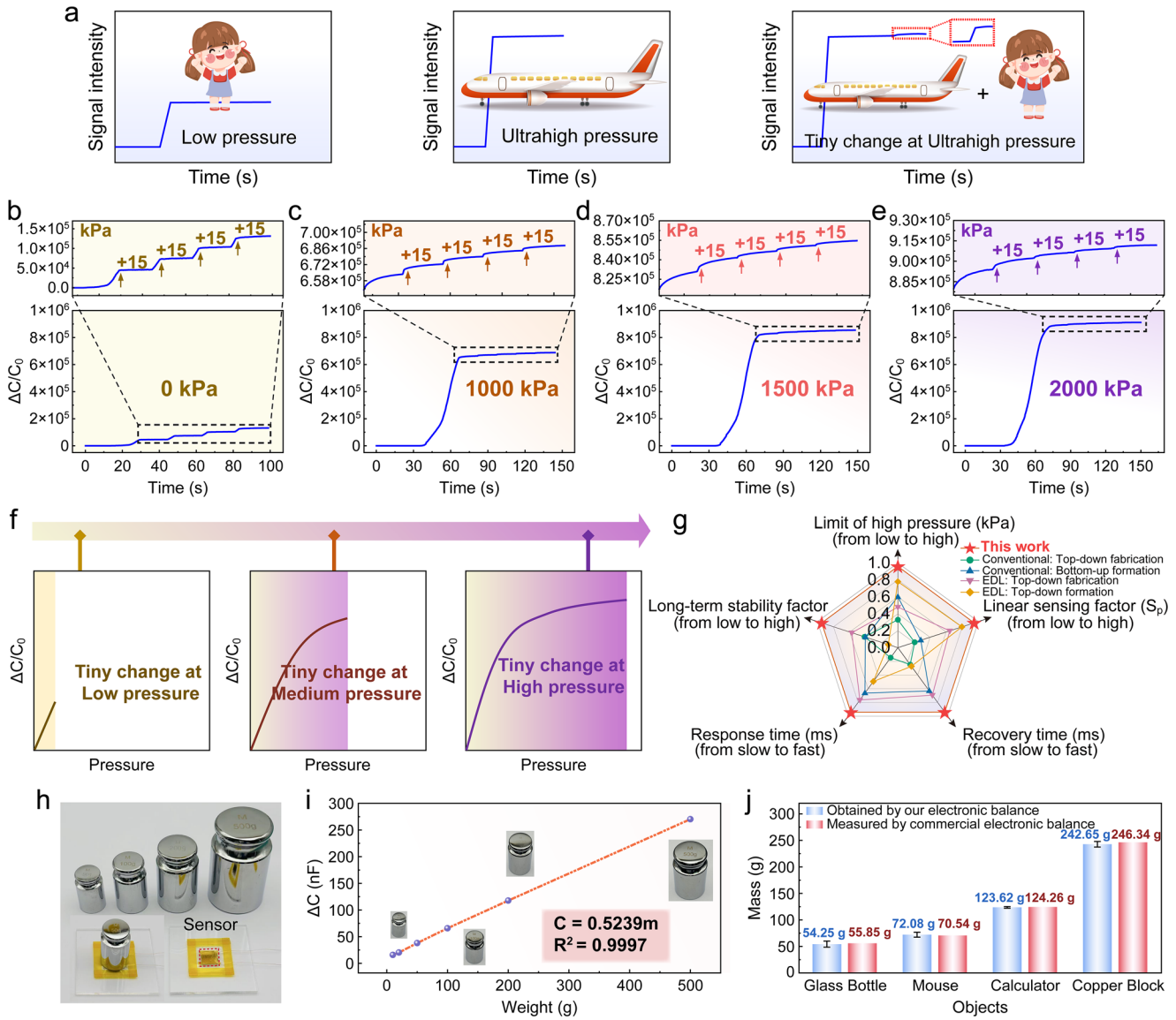

FIGURE 7 | High-resolution sensing and linear response of the Iontronic pressure sensor. (a) Schematic of iontronic sensing under low- and high-pressure preloads, illustrating detection of small pressure increments (ΔP) superimposed on high-pressure preload. (b–e) Dynamic capacitance responses to small pressure (15 kPa) steps at reference pressures of 0, 1000, 1500, and 2000 kPa. (f) Conceptual trend of response amplitude as a function of preload pressure. (g) Multidimensional performance comparison between this work and different types of capacitive pressure sensors. (h) Simple electronic balance device using sensor. (i) Calibration curve of capacitance versus mass using standard weights of 10, 20, 50, 100, 200 and 500 g. (j) Comparison between masses measured by the sensor-based balance with those obtained from a commercial electronic balance.

stepwise increase in capacitance with gradually amplified yet stable amplitudes. Even at 2.0 MPa preload, the device generates a well-resolved transient capacitance response to the 15 kPa step, with minimal noise and a minimum pressure resolution of 0.75%. These results demonstrate that the GHA sensor can clearly and stably detect subtle pressure changes under an MPa-level high preload. The conceptual response trend in Figure 7f further illustrates that, as preload increases, the GHA architecture effectively delays high-pressure saturation, allowing the sensor response to continue rising over a wider pressure span and preserving step discernibility even under MPa-level preloads-thereby validating the robustness of its structural design. As summarized in Figure 7g and Table S2, the present sensor was compared with different capacitive pressure-sensing strategies in terms of linear sensing factor, pressure detection range, response/recovery time, and long-term cycling stability. The radar profile encompasses a larger and more balanced area, indicating the coordinated improvement of multiple key sensing metrics. These results highlight the potential of the proposed design strategy for developing high-performance flexible pressure sensors.

To demonstrate the linear response in a practical scenario, we integrated the sensor into a simple electronic balance (Figure 7h). Calibration was performed using standard weights (10, 20, 50, 100, 200, and 500 g) to establish the relationship between capacitance C and mass m (Figure 7i). The fitted line $C = 0.5239m$ (m in g) yields an excellent linear correlation with $R^2 = 0.9997$. We then used this balance to weigh several everyday objects with unknown mass, including a glass bottle, a computer mouse, a

16163028, 2026, 71, Downloaded from https://advanced.onlinelibrary.wiley.com/doi/10.1002/adfm.77497 by Beihang University (Buaa), Wiley Online Library on [23/09/2026]. See the Terms and Conditions (https://onlinelibrary.wiley.com/terms-and-conditions) on Wiley Online Library for rules of use; OA articles are governed by the applicable Creative Commons License

calculator, and a copper block, each measured three times. As shown in Figure 7j, the masses obtained from our prototype agree well with those measured by a commercial electronic balance (Figure S10), with deviations from the fitted values of 2.865%, −2.193%, 0.518% and 1.496%, respectively. These small errors show that the sensor can be used for direct and accurate mass measurement without complex non-linear calibration, underscoring its practical utility and versatility.

2.9 | Practical Demonstrations of GHA-Based Iontronic Sensors from Pa-Level Touch to MPa-Level Loads

Reliable cross-scale sensing from Pa to MPa within a single device-while still distinguishing small pressure increments, maintaining good linearity, and avoiding early saturation-is highly desirable for practical applications. This ability is especially important in complex situations, like getting ready to detect tiny pressure signals under slight deformations or high static background loads. To examine this capability, we performed a series of measurements spanning micro-pressure detection to extreme high-pressure loading. In a representative micro-pressure test (Figure 8a), three mung beans (each with a mass of ≈0.077 g, corresponding to a single-digit-Pa load) were gently and sequentially placed on the sensor. The resulting capacitance traces show rapid, clearly resolved stepwise increases for each placement, indicating that the device accurately converts Pa-level mechanical stimuli into fast, well-defined electrical responses (Movie S1).

For human-motion detection, we selected the finger as a representative test site and mounted the sensor on its surface while the joint was held at different bending angles. Owing to its high flexibility and frequent involvement in fine, multi-stage movements, the finger offers a sensitive and representative platform for evaluating motion-sensing performance [69, 70]. Unlike typical finger bending demos, our device can accurately capture tiny bending changes, is highly sensitive, and responds quickly. As shown in Figure 8b,c, the device outputs clearly differentiated signal levels as the finger moves from a naturally extended state to slight bending, revealing a rapid electrical response and high sensitivity to small bending-induced strains.

High angular resolution under small bending deformation is crucial for accurately capturing subtle human-motion signatures. To quantify this capability, we implemented a precise stepwise bending protocol in which the finger joint angle was increased from 0° to 11.6° in discrete increments (Figure 8d). At each angular step, the device yields steep, highly stable step responses, and the normalized capacitance change increases approximately monotonically with bending angle. The sensor reliably resolves bending angles as small as 2.3°, indicating a low angular detection threshold with clearly discernible signal levels (Movie S2). As shown in Figure 8e, plotting the mean step amplitude against bending angle produces a linear regression relationship, confirming a well-defined and nearly linear angular response

$$\Delta C/C_0 = 0.04538\theta + 0.0273, R^2 = 0.9994 \quad (4)$$

where θ denotes the bending angle (°). These results indicate that the device exhibits an approximately linear angular response over 0–11.6°. As shown in Figure S11, even for bending angles of only a few degrees, the sensor output remains clearly distinguishable, supporting its use in applications that require monitoring minute joint motions. When the sensor is mounted on the finger joint and the angle is referenced with a goniometer (Figure 8f,g), the signal variation with bending can be directly tracked. As the finger angle increases stepwise from 0° to 90°, the peak response rises approximately linearly, and the signals corresponding to different bending states are clearly separated, indicating a stable dynamic response and high angular resolution over a wide angular range suitable for wearable electronics and human-machine interfaces.

As shown in Figure 8h, the device exhibits a stable response under extreme preloads. The sensor was mounted at the bottom of a water tank (total mass ≈8.7 kg), corresponding to a nominal pressure of ≈1.07 MPa on the sensing area. We monitored the output over ten manually controlled loading/unloading cycles; in each cycle, the capacitance response shows rapid, reversible, and stable transitions with negligible drift (Movie S3), demonstrating excellent response stability and repeatability at high-pressure. When additional water is introduced in ∼600 g increments (≈73.6 kPa per step), the output exhibits nearly linear stepwise increases (Figure 8i,j and Movie S4), achieving kilopascal-level pressure resolution on top of a megapascal-scale preload. Three independent devices demonstrated consistent performance in repeat testing (see Figure S12), confirming high resolution and long-term operational stability under high-pressure conditions. This robustness underscores their suitability for online monitoring in extreme pressure environments. These results show that our sensor is more than just an ordinary pressure sensor; it has clear advantages in some specific applications, like complex contact interfaces, robot tactile feedback, rehabilitation assessment, and detecting pressure fluctuations under high background pressure.

3 | Discussion

In summary, this work presents a scalable design strategy that integrates FEA-guided optimization with a daisy-inspired multi-level gradient hemispherical architecture to realize an iontronic pressure sensor with simultaneously high sensitivity and a broad operating range. The key advance lies in the rational coupling of hierarchical structural compressibility with programmed contact-area evolution at the ionogel/electrode interface, which enables the GHA architecture to overcome the conventional sensitivity–range trade-off. Interpretable machine learning further supports the FEA-derived design rules and provides additional insight into the structure–performance relationship governing pressure transduction in the multilevel architecture. As a consequence, the sensor achieves a high sensitivity of ≥122.13 kPa^{-1} over a wide pressure range of ≥2.555 MPa, together with excellent linearity and dynamic stability. Owing to the reduced initial contact area introduced by the fine GHA surface features, an ultrahigh sensitivity of 1864.19 kPa^{-1} is obtained below 61 kPa, with a linearity of $R^2 = 0.9993$. The device also exhibits a fast response of <5 ms at 200 kPa and stable operation over more than 5700 cycles at 1377 kPa, confirming its robust durability under

16163028, 2026, 71, Downloaded from https://advanced.onlinelibrary.wiley.com/doi/10.1002/adfm.77497 by Beihang University (Buaa), Wiley Online Library on [23/09/2026]. See the Terms and Conditions (https://onlinelibrary.wiley.com/terms-and-conditions) on Wiley Online Library for rules of use; OA articles are governed by the applicable Creative Commons License

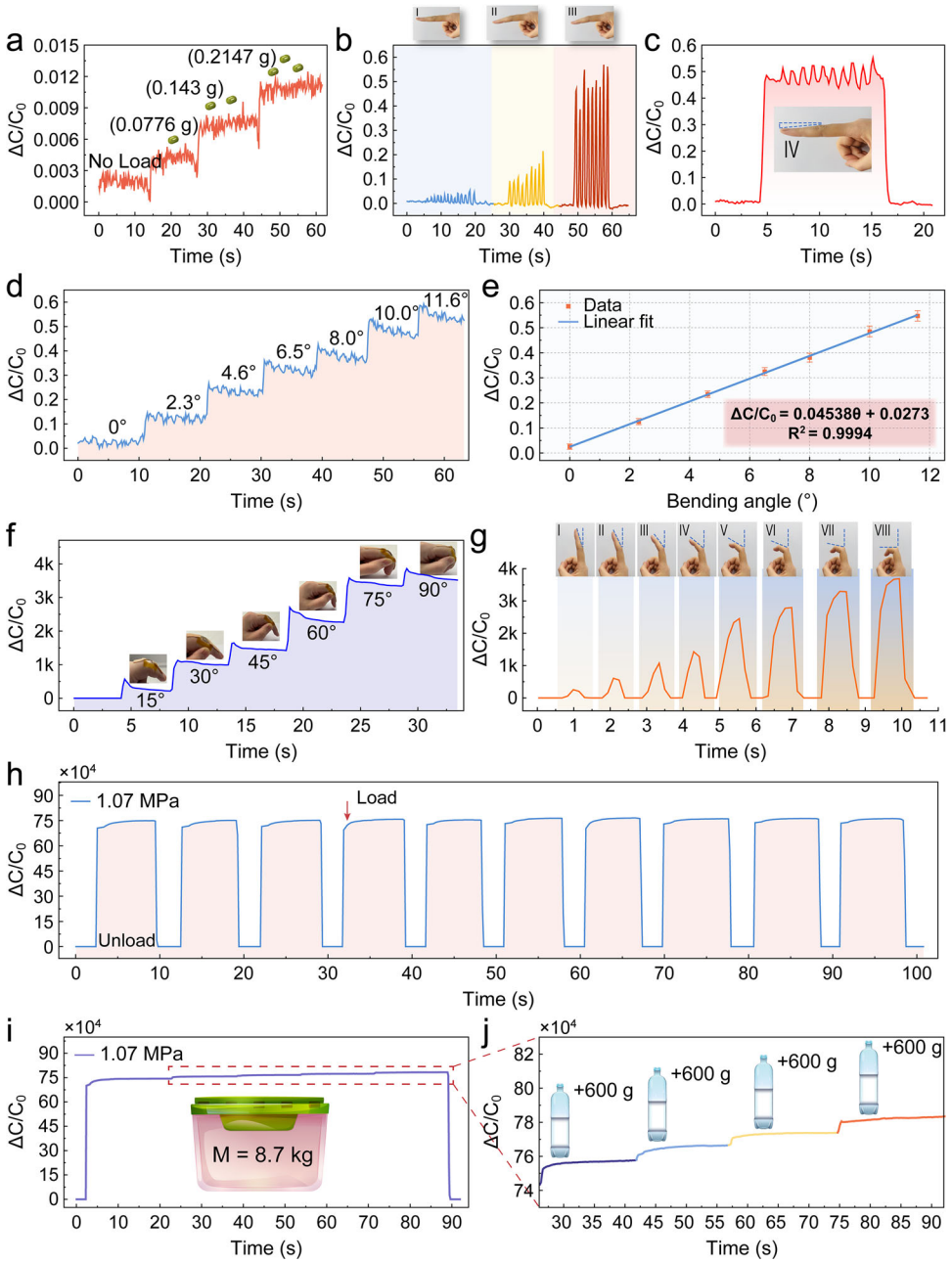

FIGURE 8 | Versatile Pressure Monitoring across the Pa-MPa range with the GHA Iontronic Sensor. (a) Sensor response to minute loads using mung beans as representative test objects (inset: measurement setup). (b,c) Real-time capacitive responses of the sensor attached to a finger under slight bending, with insets showing the corresponding finger postures. (d,e) Stepwise capacitance responses and calibration curves as a function of small bending angle θ. (f,g) Real-time responses for monitoring finger bending from slight flexion to 90° full movement. (h) Capacitive response of a water-filled tank under ten loading/unloading cycles at a static preload of ~1.07 MPa. (i,j) Stepwise responses obtained by successively adding water in 600 g increments on top of an ~8.7 kg preload.

high-pressure conditions. Application demonstrations spanning from Pa-level stimuli to MPa-level preload conditions further illustrate its versatility in subtle load detection, motion monitoring, and signal recognition under heavy loads. More broadly, this readily manufacturable strategy, which is compatible with large-area fabrication, provides a generalizable framework for engineering bioinspired microstructured interfaces and may be extended to a wide range of tactile sensing platforms for wearable electronics, robotic skins, and human–machine interaction systems.

4 | Methods

4.1 | Materials and Chemicals

Silicone rubber (PDMS, SYLGARD 184) was purchased from Dow Chemical Co. (USA). Polyethylene terephthalate/gold (PET/Au) conductive film, PVA-1799, and ethanol (AR grade) were obtained from Aladdin Industrial Corporation (China). Phosphoric acid (H_3PO_4, AR, ≥85%) was supplied by Shanghai Macklin Biochemical Co., Ltd. (China). PET film (thickness 75 μm) and PDMS

16163028, 2026, 71, Downloaded from https://advanced.onlinelibrary.wiley.com/doi/10.1002/adfm.77497 by Beihang University (Buaa), Wiley Online Library on [23/09/2026]. See the Terms and Conditions (https://onlinelibrary.wiley.com/terms-and-conditions) on Wiley Online Library for rules of use; OA articles are governed by the applicable Creative Commons License

membrane (thickness 100 μm) were purchased from Opivit New Energy Technology Co., Ltd. (China). All materials were used as received unless otherwise specified.

4.2 | Compressive Simulation by Finite Element Analysis

Finite element analysis (FEA) was conducted using the commercial software ABAQUS 2024. The microstructured PVA/H_3PO_4 ionogel film was modelled with an Ogden hyperelastic constitutive law whose parameters were obtained from standard uniaxial tensile tests (see details in Figure S13). The PET/Au electrode (elastic modulus $E \approx 3$ GPa) was treated as a rigid plate and pressed downward onto the ion-gel surface under frictionless contact. The initial contact area A_0 was determined under a preload of 250 Pa. The resulting stress distributions under different loads are shown in Figure 2, and simulation data were used to guide structural optimization of the gradient hemispherical architecture.

4.3 | Preparation of Microstructured Ionogel Film

A master template was fabricated by a projection micro-stereolithography system (microArch S230A, BMF Precision Tech, Inc., USA) to generate a mold with a periodic hemispherical array. The PDMS precursor (SYLGARD 184, Dow Corning Co., Ltd., USA) was mixed at a base-to-curing-agent ratio of 10:1, cast onto the printed resin mold, and cured at 75°C for 2 h. After curing, the patterned PDMS film was peeled off and used as the negative template for casting the microstructured ionogel film.

The pure PVA solution was prepared by dissolving 1.00 g of polyvinyl alcohol in 9.00 g of deionized water and stirring at 95°C for 2 h. The solution was then cooled to 50°C, after which 800 mL of phosphoric acid (H_3PO_4, AR, ≥85%) was added and stirring continued for 1 h. The resulting mixture was cast onto the PDMS template and cured at ambient temperature (~25°C) for 48 h. The solidified ionogel film had a thickness of approximately 50 μm and faithfully replicated the graded hemispherical array on its surface before being peeled from the PDMS template.

4.4 | Assembly of Iontronic Pressure Sensor

A magnetron sputterer (PVD 75, Kurt J. Lesker) was used to deposit a 100 nm gold layer onto flexible polyethylene terephthalate (PET) films (thickness 75 μm) to obtain PET/Au electrodes. The PET-Au films were treated by plasma and then cut into 10 × 10 mm pieces using a laser cutter. The microstructured ionogel film was sandwiched between two PET/Au electrodes to form the sensing capacitor. Finally, the assembled device was encapsulated with a 100 μm-thick PDMS film to yield the flexible iontronic pressure sensor.

4.5 | Characterization and Measurements

The morphologh of ionogel microstructures was examined by field-emission scanning electron microscopy (SU8020 Hitachi). All output capacitances were collected using a precision LCR meter (E4980A, Agilent) at a test frequency of 1 kHz, except for the response-time measurements, for which the capacitance was recorded using a high-speed LCR digital bridge (TH2840B, Tonghui) operated at 10 kHz. The resistance of the electrode was measured with a digital multimeter (VC890C, Victory). A multifunctional tension-compression testing system (YL-S71, Yueh-Lian Pressure Testing Co., Ltd.) was employed to record applied force. Cyclic loading/unloading tests were performed using a programmable linear motor (E1100, LinMot) to ensure precise and repeatable mechanical stimulation. For finger-bending experiments, the sensor was conformally attached to the finger surface to ensure intimate contact and efficient strain transfer. For weight-sensing and high-pressure-resolution measurements, the device was mounted at the edge of a cylindrical base so that normal loads could be applied via incremental mass loading. All electrical and mechanical data were processed and plotted using Origin (Origin Lab) for subsequent analysis and figure preparation.

During testing, a commercially available nitrile glove was used as an isolation layer between the skin and the sensor to avoid direct contact. All related tests were non-invasive, and no discomfort or adverse effects were observed after the experiments. The volunteer, who was also the first author of this study, provided written informed consent.

Author Contributions

C.F.P. contributed to conceptualization, project supervision, overall guidance, and manuscript revision. **B.R.J**. conceived the project, carried out the FEA simulations and experiments, analyzed the data, prepared and revised the figures, and wrote the original draft. **R.J.Z**. performed the machine learning analysis and contributed to the interpretation of the results, figure preparation, and revision of the manuscript. **W.C.G**. supervised the FEA simulations. All authors discussed the results and approved the final manuscript.

Acknowledgements

The authors thank the support of the National Key Research and Development (R&D) Program from the Ministry of Science and Technology of China (2024YFB3814100), the National Natural Science Foundation of China (No. 52125205, 52532005 and 52250398), the Natural Science Foundation of Beijing Municipality (2222088 and L223006), and the Fundamental Research Funds for the Central Universities. The authors also thank Xuzhou B&C Chemical Co. Ltd for providing the photoresist (HTA116, HTA112, B&C Chemicals) used in our work.

Conflicts of Interest

The authors declare no conflicts of interest.

Data Availability Statement

The data that support the findings of this study are available in the supplementary material of this article.

References

1. H. Hu, H. Huang, M. Li, et al., "A Wearable Cardiac Ultrasound Imager," *Nature* 613 (2023): 667–675.

16163028, 2026, 71, Downloaded from https://advanced.onlinelibrary.wiley.com/doi/10.1002/adfm.77497 by Beihang University (Buaa), Wiley Online Library on [23/09/2026]. See the Terms and Conditions (https://onlinelibrary.wiley.com/terms-and-conditions) on Wiley Online Library for rules of use; OA articles are governed by the applicable Creative Commons License

2. Y. Wang, C. Sun, and D. Ahmed, "A Smart Acoustic Textile For Health Monitoring," *Nature Electronics* 8 (2025): 485–495.

3. H. Yu, D. Sun, W. Dong, et al., "All-In-One Flexible Thermoelectric Yarns for Integrated Energy Harvesting, Adaptive Personal Thermal Management, and Self-Powered Sensing," *Advanced Functional Materials* 36 (2026): 25233.

4. R. Zhu, Z. Li, G. Deng, et al., "Anisotropic Magnetic Liquid Metal Film For Wearable Wireless Electromagnetic Sensing And Smart Electromagnetic Interference Shielding," *Nano Energy* 92 (2022): 106700.

5. M. Hassan, G. Abbas, N. Li, et al., "Significance of Flexible Substrates for Wearable and Implantable Devices: Recent Advances and Perspectives," *Advanced Materials Technologies* 7 (2021): 2100773.

6. X. Han, J. Tao, Y. Liang, et al., "Ultraweak Light-Modulated Heterostructure With Bidirectional Photoresponse For Static And Dynamic Image Perception," *Nature Communications* 15 (2024): 10430.

7. J. He, R. Wei, S. Ge, et al., "Artificial Visual-Tactile Perception Array For Enhanced Memory And Neuromorphic Computations," *InfoMat* 6 (2023): 12493.

8. X. Pan, Y. Zhuang, W. He, et al., "Quantifying the Interfacial Triboelectricity In Inorganic-Organic Composite Mechanoluminescent Materials," *Nature Communications* 15 (2024): 2673.

9. Q. Sun, P. Chen, K. Lv, et al., "Artificial Neuron Based on Electrical Anisotropy From WSe_2 Field Effect Transistors," *Advanced Science* 13 (2026): 15893.

10. Z. Yang, S. Huo, Z. Zhang, et al., "High-Precision Multibit Opto-Electronic Synapses Based on ReS_2 /h-BN/Graphene Heterostructure for Energy-Efficient and High-Accuracy Neuromorphic Computing," *Advanced Functional Materials* 35 (2025): 2509119.

11. J. He, R. Wei, X. Ma, et al., "Contactless User-Interactive Sensing Display for Human–Human and Human–Machine Interactions," *Advanced Materials* 36 (2024): 2401931.

12. W. Heng, S. Solomon, and W. Gao, "Flexible Electronics and Devices as Human–Machine Interfaces for Medical Robotics," *Advanced Materials* 34 (2022): 2107902.

13. Y. Zhao, R. Wu, Y. Hao, et al., "Eco-Friendly Multifunctional Hydrogel Sensors Enabled Sustainable and Accurate Human-Machine Interaction System," *Advanced Materials* 37 (2025): 2507127.

14. J. He, J. Huang, R. Li, et al., "Hysteresis-Free and Dynamically Resilient Strain Sensor Enabled By Interfacial Coordination," *Science Advances* 12 (2026): 2450.

15. Y. Zhao, W. Gao, K. Dai, et al., "Bioinspired Multifunctional Photonic-Electronic Smart Skin for Ultrasensitive Health Monitoring, for Visual and Self-Powered Sensing," *Advanced Materials* 33 (2021): 2102332.

16. Y. Liu, J. Tao, Y. Mo, R. Bao, and C. Pan, "Ultrasensitive Touch Sensor for Simultaneous Tactile and Slip Sensing," *Advanced Materials* 36 (2024): 2313857.

17. B. Sun, Z. Li, Z. Song, et al., "Gradient Modulus Strategy for Alleviating Stretchable Electronic Strain Concentration," *Advanced Functional Materials* 34 (2024): 2410676.

18. W. Yang, S. Liu, Z. Wang, et al., "Bioinspired Composite Fiber Aerogel Pressure Sensor For Machine-Learning-Assisted Human Activity And Gesture Recognition," *Nano Energy* 127 (2024): 109799.

19. H. Liu, X. Chen, Y. Zheng, et al., "Lightweight, Superelastic, and Hydrophobic Polyimide Nanofiber /MXene Composite Aerogel for Wearable Piezoresistive Sensor and Oil/Water Separation Applications," *Advanced Functional Materials* 31 (2021): 2008006.

20. S. Yang, W. Yang, R. Yin, et al., "Waterproof Conductive Fiber With Microcracked Synergistic Conductive Layer For High-Performance Tunable Wearable Strain Sensor," *Chemical Engineering Journal* 453 (2023): 139716.

21. J. He, S. Wang, R. Han, et al., "Wide Detection Range Flexible Pressure Sensors Based on 3D Interlocking Structure TPU/ZnO NWs," *Advanced Functional Materials* 35 (2024): 2418791.

22. L. Song, Z. Wang, S. Chen, Y. Shen, J. Yin, and R. Wang, "Phytic Acid-Induced Gradient Hydrogels for Highly Sensitive and Broad Range Pressure Sensing," *Advanced Materials* 37 (2025): 2417978.

23. J. Li, K. Guo, P. Li, et al., "High-sensitivity Capacitive Pressure Sensor Based on Novel and Bio-Inspired Hybrid Dielectric Layer For Medical Exercise Rehabilitation," *Composites Part B: Engineering* 303 (2025): 112565.

24. Y. Li, W. Zhang, C. Zhao, et al., "Breaking the Saturation of Sensitivity for Ultrawide Range Flexible Pressure Sensors by Soft-Strain Effect," *Advanced Materials* 36 (2024): 2405405.

25. H. Xu, L. Gao, H. Zhao, et al., "Stretchable and Anti-Impact Iontronic Pressure Sensor With An Ultrabroad Linear Range for Biophysical Monitoring and Deep Learning-Aided Knee Rehabilitation," *Microsystems & Nanoengineering* 7 (2021): 92.

26. X. Fu, J. Zhang, J. Xiao, et al., "A High-Resolution, Ultrabroad-Range And Sensitive Capacitive Tactile Sensor Based on a CNT/PDMS Composite For Robotic Hands," *Nanoscale* 13 (2021): 18780–18788.

27. H. Niu, Y. Chen, E.-S. Kim, W. Zhou, Y. Li, and N.-Y. Kim, "Ultrasensitive Capacitive Tactile Sensor With Heterostructured Active Layers For Tiny Signal Perception," *Chemical Engineering Journal* 450 (2022): 138258.

28. J. You, M. Lu, L. Dazhen, et al., "Anti-Motion Artifacts Iontronic Sensor for Long-Term Accurate Fingertip Pulse Monitoring," *Advanced Science* 12 (2025): 2414425.

29. Y. Xiao, X. Wu, L. Yang, and J. Zhu, "Fabrication of High-Performance Fabric-Based Capacitive Pressure Sensors With Two-Scale Synergistic Resistive/Capacitive Hybrid Response," *Journal of Materials Science & Technology* 240 (2026): 87–97.

30. L. Wu, X. Li, J. Choi, et al., "Beetle-Inspired Gradient Slant Structures for Capacitive Pressure Sensor With a Broad Linear Response Range," *Advanced Functional Materials* 34 (2024): 2312370.

31. Y. Zhang, J. Yang, X. Hou, et al., "Highly Stable Flexible Pressure Sensors With a Quasi-Homogeneous Composition and Interlinked Interfaces," *Nature Communications* 13 (2022): 1317.

32. C. Lv, C. Tian, J. Jiang, et al., "Ultrasensitive Linear Capacitive Pressure Sensor With Wrinkled Microstructures for Tactile Perception," *Advanced Science* 10 (2023): 2206807.

33. M. Song, Q. Liu, X. Xu, et al., "A Fabric-Based Multimodal Flexible Tactile Sensor With Precise Sensing and Discrimination Capabilities for Pressure-Proximity-Magnetic Field Signals," *Advanced Functional Materials* 35 (2025): 2420445.

34. X. Li, Y. Liu, Y. Ding, et al., "Capacitive Pressure Sensor Combining Dual Dielectric Layers With Integrated Composite Electrode for Wearable Healthcare Monitoring," *ACS Applied Materials & Interfaces* 16 (2024): 12974–12985.

35. H. B. Choi, J. Oh, Y. Kim, et al., "Transparent Pressure Sensor With High Linearity Over a Wide Pressure Range for 3D Touch Screen Applications," *ACS Applied Materials & Interfaces* 12 (2020): 16691–16699.

36. R. Liu, B. Ji, M. Lei, F. Hu, J. Luo, and B. Zhou, "Triple-Gradient Based Dielectric Layer For Flexible Capacitive Sensor With Broad Sensing Linearity And High Sensitivity," *Applied Materials Today* 42 (2025): 102614.

37. Y. Tagawa, S. Lee, T. Someya, and T. Yokota, "A Capacitive Pressure Sensor With Linearity and High Sensitivity Over a Wide Pressure Range Using Thermoplastic Microspheres," *Advanced Electronic Materials* 9 (2023): 2201304.

38. K. H. Ha, W. Zhang, H. Jang, et al., "Highly Sensitive Capacitive Pressure Sensors Over a Wide Pressure Range Enabled by the Hybrid Responses of a Highly Porous Nanocomposite," *Advanced Materials* 33 (2021): 2103320.

16163028, 2026, 71, Downloaded from https://advanced.onlinelibrary.wiley.com/doi/10.1002/adfm.77497 by Beihang University (Buaa), Wiley Online Library on [23/09/2026]. See the Terms and Conditions (https://onlinelibrary.wiley.com/terms-and-conditions) on Wiley Online Library for rules of use; OA articles are governed by the applicable Creative Commons License

39. G. Yang, X. Zheng, J. Li, et al., "Schottky Effect-Enabled High Unit-Area Capacitive Interface for Flexible Pressure Sensors," *Advanced Functional Materials* 34 (2024): 2401415.

40. J. Yang, G. Yuan, Y. Shen, et al., "Pushing Pressure Detection Sensitivity to New Limits by Modulus-Tunable Mechanism," *Advanced Science* 11 (2024): 2403779.

41. Y. Xia, Y. Zhu, X. Zhi, et al., "Transparent Self-Healing Anti-Freezing Ionogel for Monolayered Triboelectric Nanogenerator and Electromagnetic Energy-Based Touch Panel," *Advanced Materials* 36 (2024): 2308424.

42. X. Chen, X. Xia, and C. F. Guo, "Flexible Iontronic Sensing: Ionic Materials, Electrodes, and Encapsulation," *Advanced Functional Materials* 36 (2025): 12920.

43. J. E. Hyun, T. Lim, S. H. Kim, and J. H. Lee, "Wearable Ion Gel Based Pressure Sensor With High Sensitivity And Ultra-Wide Sensing Range For Human Motion Detection," *Chemical Engineering Journal* 484 (2024): 149464.

44. L. Li, G. Zhu, J. Wang, J. Chen, G. Zhao, and Y. Zhu, "A Flexible and Ultrasensitive Interfacial Iontronic Multisensory Sensor With an Array of Unique "Cup-Shaped" Microcolumns For Detecting Pressure And Temperature," *Nano Energy* 105 (2023): 108012.

45. D. Su, G. Shen, K. Ma, et al., "Enhanced Sensitivity and Linear-Response in Iontronic Pressure Sensors for Non-Contact, High-Frequency Vibration Recognition," *Journal of Colloid and Interface Science* 659 (2024): 1042–1051.

46. Z. Ding, W. Li, W. Wang, et al., "Highly Sensitive Iontronic Pressure Sensor With Side-by-Side Package Based on Alveoli and Arch Structure," *Advanced Science* 11 (2024): 2309407.

47. Z. He, Y. Chen, J. Li, J. Qu, L. Chen, and F. Li, "*Hofmeister* Effect Regulated Gel Iontronic Sensors for Wide-Range Pressure Perception," *The Innovation Materials* 2 (2024): 100078.

48. Y. Zheng, T. Lin, N. Zhao, et al., "Highly Sensitive Electronic Skin With A Linear Response Based On The Strategy Of Controlling The Contact Area," *Nano Energy* 85 (2021): 106013.

49. N. Bai, L. Wang, Y. Xue, et al., "Graded Interlocks for Iontronic Pressure Sensors With High Sensitivity and High Linearity Over a Broad Range," *ACS Nano* 16 (2022): 4338–4347.

50. R. Yang, A. Dutta, B. Li, et al., "Iontronic Pressure Sensor With High Sensitivity Over Ultra-Broad Linear Range Enabled By Laser-Induced Gradient Micro-Pyramids," *Nature Communications* 14 (2023): 2907.

51. C. Zhao, Y. Wang, G. Tang, et al., "Ionic Flexible Sensors: Mechanisms, Materials, Structures, and Applications," *Advanced Functional Materials* 32 (2022): 2110417.

52. H. Yuan, Q. Zhang, T. Zhou, et al., "Progress and Challenges in Flexible Capacitive Pressure Sensors: Microstructure Designs and Applications," *Chemical Engineering Journal* 485 (2024): 149926.

53. S. Ghoddousi, M. Mohammadnejad, M. Safarabadi, and M. Haghighi-Yazdi, "Compression Response of Nature-Inspired Metamaterials Based on Fibonacci Spiral," *International Journal of Mechanical Sciences* 285 (2025): 109853.

54. T. Zhang, M. Cieslak, A. Owens, et al., "Phyllotactic Patterning of Gerbera Flower Heads," *Proceedings of the National Academy of Sciences* 118 (2021): 2016304118.

55. F. Zhuo, Z. Ding, X. Yang, et al., "Advanced Morphological and Material Engineering for High-Performance Interfacial Iontronic Pressure Sensors," *Advanced Science* 12 (2025): 2413141.

56. X. Zhao, M. Yang, F. Li, et al., "A "Rigid-Flexible" Iontronic Pressure Sensor With High Sensitivity And Wide Response Range For Hand Dysfunction Rehabilitation Training," *Chemical Engineering Journal* 507 (2025): 160539.

57. L. Lv, T. Liu, T. Jiang, et al., "A Highly Sensitive Flexible Capacitive Pressure Sensor With Hierarchical Pyramid Micro-Structured PDMS-Based Dielectric Layer For Health Monitoring," *Frontiers in Bioengineering and Biotechnology* 11 (2023): 1303142.

58. J. Park, J. Kim, J. Hong, et al., "Tailoring Force Sensitivity And Selectivity By Microstructure Engineering Of Multidirectional Electronic Skins," *NPG Asia Materials* 10 (2018): 163–176.

59. P. Chytrosz-Wrobel, M. Golda-Cepa, E. Stodolak-Zych, J. Rysz, and A. Kotarba, "Effect of Oxygen Plasma-Treatment On Surface Functional Groups, Wettability, And Nanotopography Features Of Medically Relevant Polymers With Various Crystallinities," *Applied Surface Science Advances* 18 (2023): 100497.

60. N. Bai, L. Wang, Q. Wang, et al., "Graded Intrafillable Architecture-Based Iontronic Pressure Sensor With Ultra-Broad-Range High Sensitivity," *Nature Communications* 11 (2020): 209.

61. X. Guo, Y. Li, W. Hong, et al., "Bamboo-Inspired, Environmental Friendly PDMS/Plant Fiber Composites-Based Capacitive Flexible Pressure Sensors by Origami for Human–Machine Interaction," *ACS Sustainable Chemistry & Engineering* 12 (2024): 4835–4845.

62. H. Yu, Q. Wang, R. Xu, et al., "A Flexible Pressure Sensor With Wide Detection Range And High Sensitivity Based on Glycerol@phosphoric Acid Nanofibers For Human Posture Recognition Applications," *Chemical Engineering Journal* 490 (2024): 151592.

63. P. Li, L. Xie, M. Su, et al., "Skin-Inspired Large Area Iontronic Pressure Sensor With Ultra-Broad Range And High Sensitivity," *Nano Energy* 101 (2022): 107571.

64. X. Wei, H. Li, W. Yue, et al., "A High-Accuracy, Real-Time, Intelligent Material Perception System With A Machine-Learning-Motivated Pressure-Sensitive Electronic Skin," *Matter* 5 (2022): 1481–1501.

65. Y. He, Y. Cheng, C. Yang, and C. F. Guo, "Creep-Free Polyelectrolyte Elastomer For Drift-Free Iontronic Sensing," *Nature Materials* 23 (2024): 1107–1114.

66. P. Lu, L. Wang, P. Zhu, et al., "Iontronic Pressure Sensor With High Sensitivity And Linear Response Over A Wide Pressure Range Based On Soft Micropillared Electrodes," *Science Bulletin* 66 (2021): 1091–1100.

67. B. Ji, Q. Zhou, M. Lei, et al., "Gradient Architecture-Enabled Capacitive Tactile Sensor With High Sensitivity and Ultrabroad Linearity Range," *Small* 17 (2021): 2103312.

68. Y. Huang, S. Hu, Y. Li, et al., "Programmable High-Sensitivity Iontronic Pressure Sensors Support Broad Human-Interactive Perception and Identification," *npj Flexible Electronics* 9 (2025): 41.

69. K. R. Pyun, K. Kwon, M. J. Yoo, et al., "Machine-Learned Wearable Sensors For Real-Time Hand-Motion Recognition: Toward Practical Applications," *National Science Review* 11 (2024): 298.

70. P. Zhu, Z. Li, J. Pang, P. He, and S. Zhang, "Latest Developments and Trends in Electronic Skin Devices," *Soft Science* 4 (2024): 17.

Supporting Information

Additional supporting information can be found online in the Supporting Information section.

Supporting File 1: adfm77497-sup-0001-SuppMat.docx.

Supporting File 2: adfm77497-sup-0002-MovieS1-S4.zip.

16163028, 2026, 71, Downloaded from https://advanced.onlinelibrary.wiley.com/doi/10.1002/adfm.77497 by Beihang University (Buaa), Wiley Online Library on [23/09/2026]. See the Terms and Conditions (https://onlinelibrary.wiley.com/terms-and-conditions) on Wiley Online Library for rules of use; OA articles are governed by the applicable Creative Commons License